Check for updates

Water confinement in hierarchical porous silica and titania†

Pierrick Gaudin,[a] Yohann Vuillemard,[b] Florian Jonas,[a] Sabine Bouguet-Bonnet [iD] ‡*[b] and Jean-Luc Blin [iD] §*[a]

In this study, water confinement in hierarchical porous silica and titania is investigated using NMR relaxometry techniques. Results show a greater interaction of water with the TiO$_2$ surface than with the SiO$_2$ one. However, regardless of the matrix, the porosity shows no effect on water relaxation. For silica-based materials, two regimes are observed. The first one at low frequency corresponds to a surface diffusion phenomenon and the second one at high frequency is due to the motion of molecules located in a layer of water further from the surface. Concerning mesostructured titania, water relaxation is governed by very slow surface diffusion.

1. Introduction

Due to their applications in energy conversion and storage, catalysis, sensing, adsorption and separation, ordered mesoporous oxides such as SiO$_2$, TiO$_2$, ZrO$_2$, Al$_2$O$_3$, *etc.* have attracted much attention over the past few years.[1,2] In almost all of these applications, the surface properties as well as the diffusion phenomena are of much importance.[3] Among the various oxides, mesostructured silica was firstly and extensively studied thanks to the easy control of the hydrolysis–condensation rate of the precursor (silicon alkoxide).[4–7] Later, much effort was devoted to the synthesis of other mesostructured metal oxides such as TiO$_2$, Al$_2$O$_3$, F$_2$O$_3$ and others,[1,8–11] exhibiting different surface properties than silica, thereby opening new perspectives for mesostructured porous materials.[12,13] More specifically, titania is well known for its (photo)catalytic properties.[14,15] However, the synthesis of thermally stable mesostructured titania is not straightforward.[16] We have reported an original method, based on the combination of liquid crystal templating (LCT) and evaporation induced self-assembly (EISA) mechanisms, followed by ammonia treatment,[17,18] for the synthesis of mesostructured titania exhibiting an amorphous or a semi-crystalline framework.

With the goal of improving catalyst and/or adsorbent efficiency, much effort was devoted to the introduction of hierarchized porosity aiming to favor the diffusion of reactants toward the internal porosity of materials.[19,20] The resulting materials exhibit multi-modal porosities ranging from several angstroms to hundreds of micrometers.[21] Over the past few years, the development of these hierarchically porous structures at multiple length scales has attracted much attention. Meso–macroporous materials have been synthesized, using multiple templates, such as latex spheres, solid lipid nanoparticles and emulsions based on soft or hard templating methods.[22–28] For example, we reported the preparation of macro–mesoporous silica based on fluorinated emulsions.[29] In that case, we start from oil-in-water emulsion where the oil droplets are dispersed in the continuous phase that is a direct microemulsion. The oil droplets are stabilized using surfactant molecules. Upon the addition of the inorganic precursor, its polymerization occurs around the oil droplets but also around the swelled micelles by oil, which constitute the microemulsion. After hydrothermal treatment and organic removal, the obtained material exhibits porosity at two levels: the macropores (from 1.0 to 3.0 μm), which are the imprints of the emulsion oil droplets, and the mesopores (7.5 nm) which are formed by the micelles according to the cooperative templating mechanism.[29] We have also reported the synthesis of dual mesostructured titania templated by a mixture of hydrogenated (Pluronic P123) and fluorinated [R$_8^F$(EO)$_9$] porogens. These materials present two mesopore size distributions, one centered around 7.7 nm and the second around 2.3 nm.[30]

Some of the applications mentioned above impose critical conditions on the materials; for instance, in catalysis, the regeneration of catalysts is often realized at high temperatures under steam and in the presence of water or even moisture; due

[a] *Université de Lorraine, CNRS, L2CM, F-54500 Nancy, France.*
  E-mail: Jean-Luc.Blin@univ-lorraine.fr
[b] *Université de Lorraine, CNRS, CRM2, F-54500 Nancy, France.*
  E-mail: Sabine.Bonnet@univ-lorraine.fr
† Electronic supplementary information (ESI) available. See DOI: https://doi.org/10.1039/d5nj02729b
‡ Université de Lorraine, CRM2, UMR7036, Faculté des Sciences et Technologies, BP 702309, F-54506 Vandoeuvre-lès-Nancy cedex, France
§ Université de Lorraine, L2CM UMR CNRS 7053, Faculté des Sciences et Technologies, BP 70239, F-54506 Vandoeuvre-lès-Nancy cedex, France.

to the hydrolysis by water adsorbed on the surface OH groups, a structure collapse is possible. Therefore, it is essential to investigate in detail the behavior of water confined in porous networks. To reach this goal, NMR relaxometry is a powerful technique. Indeed, it can determine the relaxation rate of nuclear spins in fluid molecules within the porous medium to study both the pore characteristics (dimensions and surface properties) and the confined fluid.[31] In this study, we have used this technique with the aim of understanding the effect of both surface properties and porosity on the diffusion and interaction of water with the surface in porous materials. To investigate the influence of the inorganic framework nature, both porous SiO_2 and TiO_2 have been prepared. To study the effect of porosity, mesostructured SBA-15, macro–mesoporous silica, and mesostructured titania having small, large and dual mesopores have been considered.

2. Materials and methods

The Pluronic P123 triblock copolymer $(EO)_{20}(PO)_{70}(EO)_{20}$, titanium isopropoxide $Ti(OiPr)_4$, tetrametoxysilane (TMOS), HCl (37%) and absolute ethanol were supplied from Aldrich. The fluorinated surfactants were kindly provided by DuPont. They have an average chemical structure of $C_8F_{17}C_2H_4(OC_2H_4)_9OH$ and $C_7F_{15}C_2H_4(OC_2H_4)_8OH$. They are labeled as $R_8^F(EO)_9$ and $R_7^F(EO)_8$, respectively.

2.1. Materials preparation

2.1.1. Silica materials

SBA-15. 2.65 g of Pluronic 123 were dissolved in 100 mL of aqueous HCl at pH = 0 (1 mol L^{-1}) at 40 °C under stirring. After complete dissolution of P123, 4.22 g of TMOS were added in the solution. After 30 min, the mixture was transferred to an autoclave in an oven at 40 °C for 24 h. Afterwards, the temperature was increased up to 100 °C for 24 h. The mixture was then filtered and the surfactant was removed by ethanol extraction for 24 h (Soxhlet).

Macro–mesoporous silica (MM-SiO_2). MM-SiO_2 was synthesized according to a protocol previously reported[29] through the emulsions templating mechanism. However, due to a batch change of the $R_7^F(EO)_8$ surfactant, in this work, the emulsion was formulated from a mixture containing 30 wt% $R_8^FEO_9$ and 70 wt% of $R_7^FEO_8$. Before the incorporation of oil (perfluorodecalin), a micellar solution was prepared, containing 25 wt% of the surfactant mixture in water at pH = 0.3. The concentration of perfluorodecalin added to the micellar solution is 20 wt%. TMOS, used as the silica source, was added dropwise. The surfactant/silica molar ratio was fixed to 0.5. The obtained gel was sealed in Teflon autoclaves and heated during 24 hours at 100 °C. The final product was recovered after ethanol extraction with a Soxhlet apparatus during 48 hours.

2.1.2. Titania mesostructured materials

Large pore mesostructured titania. Large pore mesostructured titania, denoted as L-TiO_2, was synthetized following a method developed by our group.[17,18] 1 g of Pluronic 123, 20 mL of ethanol, 2 g of HCl (VWR, 37%) and 3 g of titanium isopropoxide (Sigma-Aldrich, 99%) were mixed together under vigorous stirring for 2 h. The solution was evaporated under vacuum (25 mbar, 55 °C). The resulting hybrid mesophase was submitted to a NH_3 atmosphere overnight to improve the condensation reaction. Surfactant removal was realized by solvent extraction (soxhlet). The resulting amorphous mesostructured titania was then split in two parts: one part was kept unchanged (amorphous) and denoted as L-TiO_2-A, and the other part was calcined at 380 °C (ramp 1 °C min^{-1}) under synthetic air for 1 h in a tubular quartz reactor under, yielding a semi-crystalline (small anatase particles embedded in amorphous TiO_2 walls) material denoted as L-TiO_2-SC.

Small pore mesostructured titania. Small pore mesostructured titania, denoted as S-TiO_2, was synthetized following the same protocol as that of large pore mesostructured titania except that Pluronic 123 was replaced with the $R_8^FEO_9$ fluorinated surfactant.[18] Similar to L-TiO_2, the amorphous S-TiO_2 material was split in two parts, one was calcined at 380 °C, yielding S-TiO_2-A (amorphous) and S-TiO_2-SC (semi-crystalline) materials, respectively.

Dual mesoporous titania (S&L-TiO_2). Dual mesoporous titania exhibiting both small and large mesopores (S&L-TiO_2) was synthetized according to a similar protocol[30] but by mixing 0.5 g of $R_8^FEO_9$ with 0.5 g of Pluronic 123. One part of the resulting amorphous material (S&L-TiO_2-A) was calcined yielding the semi-crystalline material S&L-TiO_2-SC.

2.2 Characterization methods

2.2.1. SAXS.
SAXS characterization studies were performed using a SAXSess mc2 (Anton Paar) apparatus equipped with a CCD detector (Princeton Instruments, 2084 × 2084 pixels array with 24 × 24 μm^2 pixel size). An X-Ray beam was provided using an ID 3003 laboratory X-ray generator equipped with a sealed X-ray tube (PANalytical, λCu (Kα) = 0.1542 nm, V = 40 kV, I = 50 mA). The distance between the sample holder and the detector was 309 mm. The X-ray signal was recorded for q ranging from 0.3 to 5 nm^{-1} with acquisition times ranging from 1 to 5 minutes.

2.2.2. Manometry nitrogen adsorption/desorption.
N_2 adsorption–desorption isotherms were determined using a Micromeritics TRISTAR 3000 sorptometer at −196 °C. Prior analyses, samples were outgassed at 25 °C under vacuum (0.13 bar) for 16 hours. The specific surface area was obtained by using the BET model whereas the pore diameter and the pore size distribution were determined by the BJH (Barrett, Joyner, Halenda) method applied to the adsorption branch.[32]

2.2.3. Mercury intrusion.
Macropores were detected using mercury porosimetry with a Micromeritics Autopore IV 9500. The penetrometer (stem volume = 0.412 mL, penetrometer volume = 1 mL) was filled with 0.1 g of the sample. A low pressure analysis (0.1 to 15 psia) followed by a high-pressure analysis (15 to 60 000 psia) were performed in order to detect

pores down to 5 nm in diameter, and the equilibration time was 10 seconds.

2.2.4. SEM. Scanning electron microscopy (SEM) micrographs were obtained using the secondary electron detector of a JEOL JCM-6000 microscope (an acceleration voltage of 15 kV).

2.2.5. Relaxometry. Porous materials were dried for 24 hours at 120 °C before hydration with a volume of degassed distilled water corresponding to a filling degree f of 80% vol. Samples were then kept at 25 °C for 1 night for complete equilibrium before ^{1}H relaxometry measurements. Samples were prepared in 8 mm o.d. hermetically sealed capsules in order to avoid any water loss during the measurements.

Proton transverse relaxation times T_2 were measured at 25 °C using a Bruker Minispec MQ20 analyzer operating at 20 MHz (^{1}H Larmor frequency). The CPMG (Carr Purcell Meiboom Gill) pulse sequence was used with an echo time of 85 μs and an acquisition of 2000 echoes. 16 scans were performed with a recycle delay of 5 s. The full magnetization decay profile was then Laplace inversed with the UPEN-WIN software.[33]

^{1}H NMRD profiles (*i.e.*, the longitudinal relaxation rate R_1 as a function of the proton Larmor frequency) were acquired between 5 kHz and 10 MHz using a Stelar Smartracer fast-field-cycling relaxometer (Stelar company, Medde, Italy). The temperature was fixed at 25 °C. For all R_1 measurements, magnetization recovery curves were found to be monoexponential within the experimental errors. 32 different values of the static magnetic field were sampled, with a fixed acquisition field of 7.2 MHz (^{1}H Larmor frequency). Pre-polarized measurements were done between 5 kHz and 4 MHz with a polarization duration of 0.6 s at a ^{1}H frequency of 8 MHz, and the non-polarized sequence was used between 4 MHz and 10 MHz. The field-switching time was 3 ms. For each B_0 value, R_1 values were obtained from the magnetization monoexponential evolution as a function of the time, sampled with 16 values between 0.01 and 4 times the longitudinal relaxation time. 32 accumulations were used for all measurements and a recycle delay of 3 s was applied.

3. Results and discussion

3.1. Structural and textural characterization

The SAXS patterns of materials are reported in Fig. 1. The SBA-15 pattern is the characteristic of the hexagonal symmetry with three characteristic diffraction peaks located at 11.02, 6.16 and 5.37 nm assigned to (100), (110) and (200) diffraction planes, respectively. The SAXS pattern of MM-SiO$_2$ exhibits only one broad diffraction peak of weak intensity at 9.24 nm, attributed to a worm-like organization of mesopores.[29] The SAXS pattern of L-TiO$_2$-A shows a well-defined peak at 10.47 nm assigned to the (100) diffraction plane, and a broad diffraction peak in the range of 6.68–4.33 nm attributed to (110) and (200) diffraction planes.[18] The broad diffraction peak observed at 4.87 nm for S-TiO$_2$-A confirms the presence of vermicular pore organization. S&L-TiO$_2$-A exhibits a SAXS diffraction pattern similar to L-TiO$_2$-A with a less defined diffraction peak at 13.96 nm and a broad
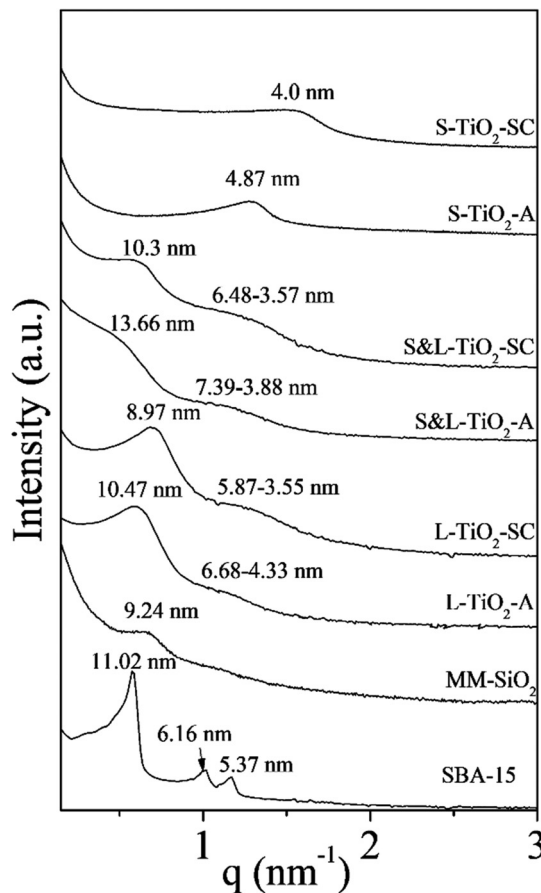

Fig. 1 SAXS patterns of the prepared materials.

peak in the 7.39–3.88 nm range that is actually the overlay of the diffraction peaks of the large pore network (100 and 110 planes) and the small pore network (vermicular organization).[30] All the SAXS patterns of calcined TiO$_2$ materials (Fig. 1) exhibit a slight shift to lower d values as compared to their parent amorphous material. Such a phenomenon is assigned to the contraction of the mesoporous network, resulting from the Ti–OH condensation and the partial crystallization of amorphous titania into anatase during the calcination step as observed by Raman and XRD in our previous studies.[17,18,30]

Nitrogen physisorption isotherms and BJH pore size distribution (insert) are reported in Fig. 2.

The porous features of prepared materials are shown by manometry nitrogen adsorption/desorption experiments (Fig. 2). Indeed, SBA-15 shows a type IV isotherm according to the IUPAC classification[32] with a well-defined hysteresis loop with two parallel and vertical branches, the characteristic of a narrow pore size distribution. The pore size is narrow (insert of Fig. 2) and centered on 9.5 nm. The L-TiO$_2$-A and L-TiO$_2$-SC materials exhibit similar type IV isotherms, but with a more extended capillary condensation zone (as compared to SBA-15) that reveals a broader pore size distribution (insert of Fig. 2) centered on 7.7 and 6.5 nm, respectively. The isotherms of S-TiO$_2$-A and of S-TiO$_2$-SC suggest super-microporous materials, *i.e.*, the pore size is located at the limit between the micro and mesoporous domains.[34] This is confirmed
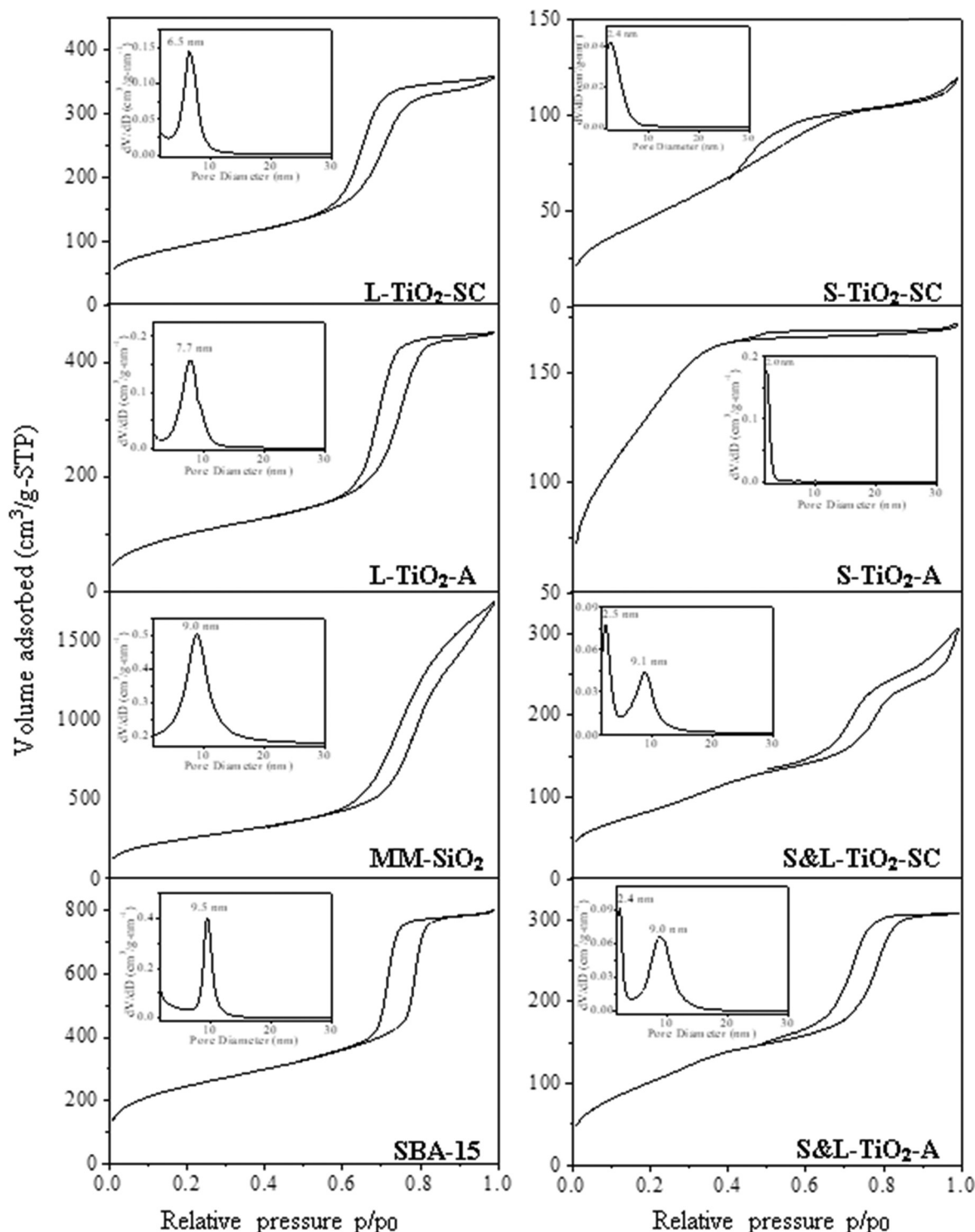
Fig. 2 Nitrogen adsorption–desorption isotherms and BJH mesopore size distributions (insert) of the prepared materials.

by the pore size distributions, in which maxima are at around 2 and 2.4 nm for S-TiO$_2$-A and S-TiO$_2$-SC, respectively. The isotherms of S&L-TiO$_2$-A and S&L-TiO$_2$-SC show two inflection points on their adsorption branch (Fig. 2). Since the pore diameter is related to the relative pressure *via* the Kelvin equation, it indicates the presence of mesopores with two different diameters. The dual mesoporosity of these mesostructured titania is also shown by their mesopore size distributions, for which two maxima at around 2.4–9.0 nm and 2.5–9.1 nm are clearly observed (the inset of Fig. 2). Finally, the adsorption–desorption isotherm of the MM-SiO$_2$ material can be defined as the combination of type II and type IV isotherms featuring the dual macro–mesoporosity of this

silica material. The mesoporous pore size distribution ranging from approximately 4 to 16 nm is broader than that for the SBA-material and its maximum is located at 9.0 nm (the inset of Fig. 2). Mercury intrusion results (Fig. 3A) confirm the presence of macropores centered on 120 nm and 4 μm. The macropores are also observed on the SEM micrographs, which show silica particles with a sponge-like structure (Fig. 3B) and having macropores with a size ranging from <1 μm up to ∼3 μm, which does not exhibit any organization.

The values of the specific surface area, the pore volume and the mesopore diameter ($\varnothing$) of the prepared materials are gathered in Table 1.

After calcination of the titania materials at 380 °C, the specific surface area decreases due to the condensation of the OH groups. Indeed, the walls of the extracted mesostructured titania are composed of the amorphous phase, which contains Ti–OH groups. Upon calcination, the condensation of these hydroxyl groups occurs.

### 3.2. Investigation of water confinement in the pore network

In order to understand the influence of pore size(s) and surface properties on water mobility inside the different materials, NMR relaxometry measurements were done. First, the transverse relaxation time T_2 measured at a proton frequency of 20 MHz was used to compare the pore size distribution of the different samples. Results are shown in Fig. 4.

The T_2 values on the order of ms clearly show the effect of confinement in these materials. Indeed, in comparison, bulk water, which is highly mobile, has relaxation times on the order of s at the same temperature and same magnetic field. Because long T_2 values come from large pores and short T_2 values come from small pores, this T_2 distribution is a model of the pore size

Table 1 Specific surface area (S_{BET}), pore volume (V_p) and mesopore diameter ($\varnothing$) of the SiO$_2$ and TiO$_2$ samples

Material	S_{BET} (m^2 g^{-1})	V_p (cm^3 g^{-1})	$\varnothing$ (nm)
SBA-15	868	1.24	9.5
MM-SiO$_2$	931	2.71	9.0
L-TiO$_2$-A	371	0.70	7.7
L-TiO$_2$-SC	337	0.56	6.5
S&L-TiO$_2$-A	387	0.48	2.4–9.0
S&L-TiO$_2$-SC	308	0.48	2.5–9.1
S-TiO$_2$-A	490	0.27	2.0
S-TiO$_2$-SC	180	0.19	2.4

distribution in the material. Indeed, relaxometry uses the enhanced relaxation of molecules at a pore surface to estimate the pore diameter. A rapid exchange between molecules at the surface and in the pores is assumed,[35] and the inverse spin–spin relaxation rate ($1/T_2$) is then proportional to the surface to volume ratio of the porous media.[36,37] The proportionality factor is called relaxivity. By fitting a distribution of relaxation times to the raw measured relaxation data, a pore size distribution can be estimated. In the case of SiO$_2$ materials, Fig. 4a shows a clear distinction between the monomodal SBA-5 and the MM-SiO$_2$, which has two T_2 distributions, reflecting two pore size distributions, *i.e.*, a bimodal network. This confirms the macro–mesoporous structure detected by nitrogen adsorption–desorption isotherms and mercury porosity. For TiO$_2$, however, it is more difficult to distinguish the *meso* from the *meso–meso* structures (Fig. 4), due to the fact that the pore sizes are of the same order of magnitude between the L-TiO$_2$ and S&L-TiO$_2$ samples (see Table 1). On the other hand, both samples show a narrowing of the T_2 distribution after calcination (Fig. 4b and c), confirming the organization of the pores and the appearance of a semi-crystalline network. Finally, it
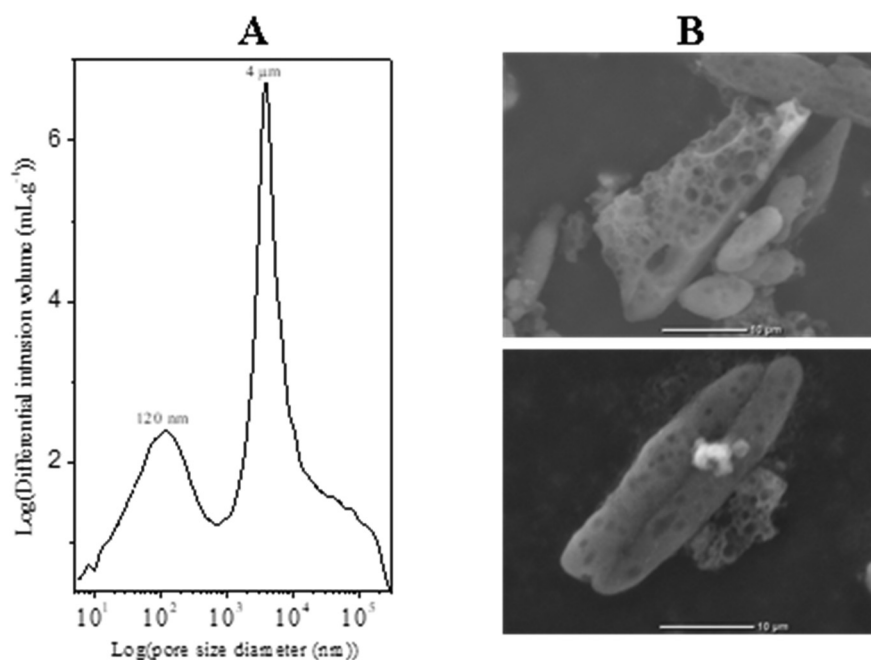
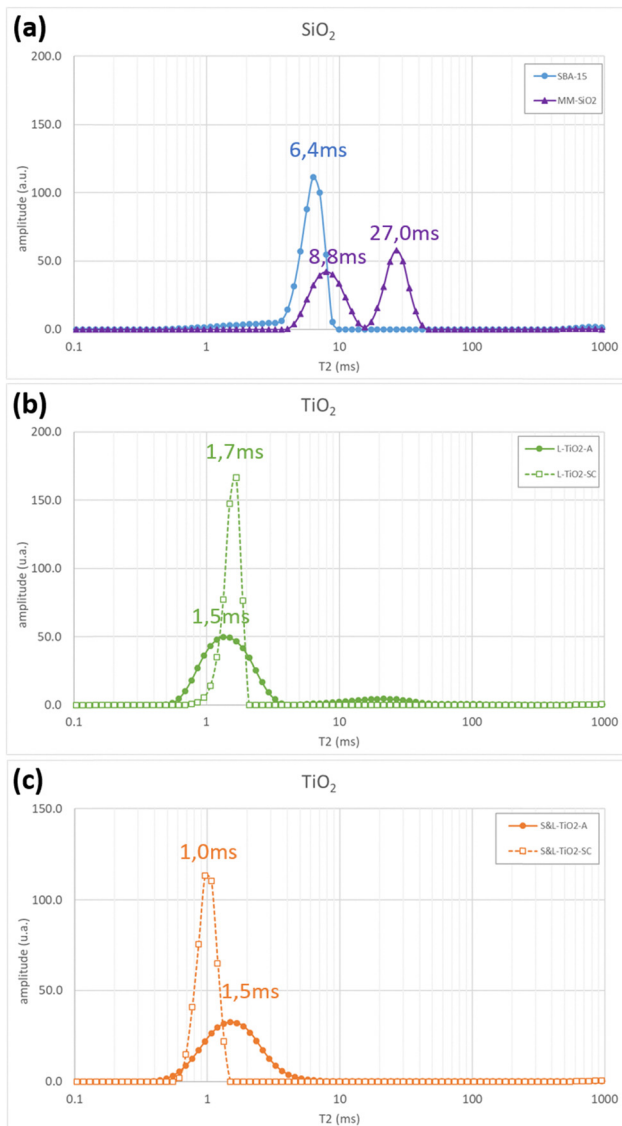**Fig. 3** Mercury intrusion porosity (A) and SEM micrographs (B) of the MM–SiO$_2$ material.

Fig. 4 ^1H T_2 distribution in silicate (a), L-TiO$_2$ (b) and S&L-TiO$_2$ (c) porous materials.

appears that the surface relaxivity of TiO$_2$ is greater than the one of SiO$_2$, as the mean T_2 is shorter in TiO$_2$ for similar pore sizes in the mesoporous network between silica and titanium samples (comparing particularly silicate and S&L-TiO$_2$). This can be attributed to a greater interaction of water with the TiO$_2$ surface.

Fast field cycling (FFC) NMR relaxometry was then used to further understand the water dynamics in these pores. FFC NMR relaxometry is a low-field NMR technique which measures the longitudinal relaxation rate, $R_1 = 1/T_1$, as a function of magnetic field strength over a wide range of frequencies.[38,39] No distribution can be measured with T_1 here because it is mainly influenced by slow molecular motions and the efficiency of energy exchange with the lattice. The latter is still sensitive to confinement, but often less dramatically than T_2, which is typically more sensitive to local magnetic field inhomogeneities and surface interactions, making it very sensitive to pore size

distributions. The FFC technique allows the information to be obtained about the molecular dynamics of water embedded in various porous materials studied here, and is particularly useful in the case of slow molecular dynamics, which can only be accessible at very low magnetic field strengths.[40]

Fig. 5 and 6a show the dispersion curves obtained on the hydrated porous samples in log–log scale. A significant variation of the longitudinal relaxation rate with the measurement frequency is observed, clearly indicating a water confinement effect in these media, and a strong interaction between water and the porous surface.[41] A first comparison of the material type shows that the relaxation rates of TiO$_2$ are about ten times greater than those of silica, irrespective of the frequency. The water–surface interactions are therefore greater for TiO$_2$ than for SiO$_2$, as expected from the transverse relaxation values. All dispersion curves can be described by power laws ($R_1 \propto \omega^{(-\alpha)} = (2\pi\nu_H)^{(-\alpha)}$) characteristic of fluids confined in rigid porous structures.[41–44] In these systems, the dispersion originates from the reorientation of the adsorbed molecular phase. The most commonly proposed mechanism is the "reorientation by translational displacements" (RMTD),[31,41,45,46] which is governed by intramolecular dipolar interactions. In this case, molecular reorientation occurs *via* surface diffusion, *i.e.*, water molecules are adsorbed on and desorbed from the surface and move on the surface by translational diffusion resulting in changes in their orientation at the same time.[45–51] The power-law exponent of the R_1 dispersion could be linked to surface dimensionality for molecules like dimethylsulfoxide and malononitrile confined in porous glass B10.[51] Regarding confined water, whose unique properties arise from its high polarity, previous studies have shown that stronger water–surface interactions lead to a steeper R_1 dispersion.[41,42,52] Consequently, it is assumed that the exponent α of the resulting dispersions power-law dependence can vary depending on the average adsorption time at the surface: the shorter the adsorption time is, the weaker the dispersion will be (*i.e.*, the smaller the value of α).[47,52] Two regimes can be clearly identified for the silica-based materials (Fig. 5). The low frequency part (<0.1 MHz) corresponds to a very slow motion resulting from a surface diffusion phenomenon, identical for both samples, SBA-15 and MM-SiO$_2$. The higher frequency part shows less dispersion, which may
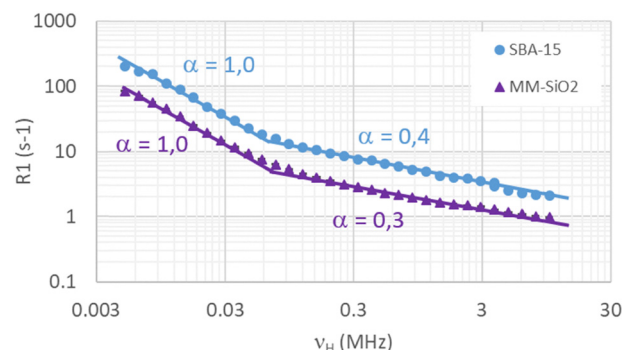

Fig. 5 ^1H longitudinal R_1 NMRD profiles in silicate porous materials at 25 °C in the frequency range of 0.005–10 MHz.
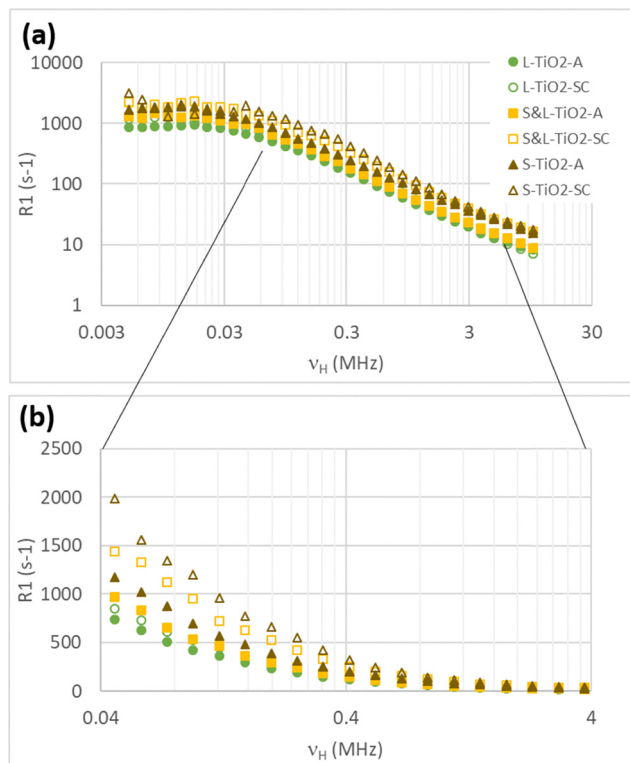
Fig. 6 (a) ^{1}H longitudinal R_1 NMRD profiles in TiO$_2$ porous materials at 25 °C in the frequency range of 0.005–10 MHz. Power law exponents obtained between 0.04 and 4 MHz equal α = 0.85 ± 0.05 for the three non-calcinated samples and α = 0.90 ± 0.05 for the three calcinated samples. (b) Zoom in semi-log scale of the frequency range of 0.04–4 MHz.

indicate the superposition of a second, faster, motion, corresponding to a water layer further from the surface and therefore less sensitive to surface interactions. This second population, in exchange with the first one, could also be ascribed to water molecules interacting with different surfaces.[50,53]

For titanium-based materials, the dispersion is very large and a single straight line is visible above 50 kHz in the log–log plot (Fig. 6a), indicating that water relaxation in these materials is largely dominated by surface diffusive motions. A rapid exchange between molecules at the surface and in the pores is assumed.[35] The fact that this rate is much higher than the usual value of 0.4 s^{-1} observed for water alone shows that this fast exchange persists at a frequency of 10 MHz. Moreover, the expected plateau at high frequency[54] is not reached here because of the spectrometer limitation. The differences between the curves obtained with the three morphologies are minimal (α = 0.85 ± 0.05 for the three samples). Although the RMTD model foresees the occurrence of a plateau at low frequency,[41,50,54,55] it should be noted that the plateau of the R_1 data obtained below 50 kHz is not taken into account here, since the T_1 values obtained (of the order of 1 ms) are lower than the field switching time used during the measurements (3 ms). Thus, the dynamics of water in TiO$_2$ materials seems to be dominated by very slow surface diffusion, which is only slightly influenced by the morphology of the material. More interestingly, calcination affects the materials S&L-TiO$_2$ and S-TiO$_2$: α

increases slightly (from 0.85 to 0.90), but above all, the values of R_1 increase on average by 70% (Fig. 6b); however, the material L-TiO$_2$ shows no significant change after calcination. The very small variation in the α coefficient, combined with an increase in relaxation homogeneously along the range of measurement frequencies, could indicate that calcination mainly causes a change in the surface properties of the materials. Indeed, the change in the interaction of water with the surface may be due to condensation of surface OH groups. Please note that the increase in R_1 values after calcination could also be explained by a decrease in the pore size of the system, as evidenced by SAXS. However, this shrinkage would mainly affect one of the mesoporous networks in the bimodal system, as there is no visible change in relaxation for the monomodal mesoporous sample.

Silica and titania are commonly used as supports or catalysts in heterogeneous catalysis. For instance, mesoporous SiO$_2$ based catalysts are used for biomass valorization.[56] However, they suffer from low hydrothermal stability and leaching of the acid groups, necessary for the catalytic reactions, occurs because of the presence of large amounts of water in biomass feedstock.[56] Concerning titania, it is a semiconductor widely used for applications not only in electronics and electrochemical systems but also as catalysts, promoters or carriers for metals and their complexes.[57–59] In particular, it is one of the most commonly used photocatalysts.[60,61] Water molecules are involved in almost all of these applications, and their interactions with the surface of TiO$_2$ strongly affect the efficiency of the titania materials.[62] More generally, since photocatalysis and catalysis are surface processes, the determination of how a molecule interacts with the surface and the quantification of the strength of these interactions are key parameters to develop efficient catalysts. Results obtained here, concerning the interaction of water with the silica and the titania matrix, will contribute to shed some lights on their hydrothermal stability upon the catalytic reaction such as the photodegradation of dyes using mesostructured TiO$_2$. The methodology can also be adapted to gas reactions, such as the oxidation of volatile organic compounds, to characterize the hydrocarbon gas dynamics as reported for methane within various solids such as carbons or zeolites.[63,64]

Moreover, the transport of the reactant and product to and from the active sites is another parameter that will affect the efficiency of the catalyst, and the characterization of the motion of the fluid molecules in the pores is needed. The latter will be facilitated by introducing a second level of porosity. Indeed, the hierarchal combination of pores can reduce transport limitations and blockage, resulting in higher activities and better control over selectivity.[65] Therefore, the information obtained concerning the surface diffusion is important to better study the reactivity of the hierarchical catalysts.

4. Conclusions

In the present study, to investigate water confinement in porous matrixes, mesostructured SBA-15, macro–mesoporous silica and mesostructured titania having small, large and dual

mesopores have been first synthesized through the self-templating mechanism. After their characterization by small angle X-ray scattering (SAXS), manometry nitrogen adsorption/desorption and scanning electron microscopy (SEM), low-field NMR relaxometry experiments have been performed.

The dispersion curves are described by power laws (straight lines in log–log representation), the characteristic of fluids confined in rigid porous media. The longitudinal relaxation rates R_1 determined for titania are greater than those obtained for silica, indicating that water–surface interactions are more important in the case of mesostructured TiO_2.

Concerning porous silica, the dispersion curves obtained on the hydrated porous samples show at low frequency a first very slow diffusive surface movement, on which is superimposed a faster movement visible above 0.1 MHz. The latter is attributed to a water layer further from the surface. Regarding titania, water relaxation is dominated by surface effects and no significant difference between materials with monomodal and those with dual mesoporosity could be noted. Results obtained in this article are of potential interest in the field of heterogeneous catalysis, where NMR relaxometry can allow further insights into surface dynamics to be obtained. This technique can provide useful information for elucidating mechanistic influences of solvents on catalyst activity and stability during the reaction.

Author contributions

Pierrick Gaudin: investigation. Yohann Vuillemard: investigation. Florian Jonas: investigation. Sabine Bouguet-Bonnet: writing – original draft and supervision. Jean-Luc Blin: writing – original draft and supervision.

Conflicts of interest

There are no conflicts to declare.

Data availability

All data are included in the manuscript. If reviewers want additional data, they will be provided by the authors upon request.

References

1 Y. Ren, Z. Ma and P. G. Bruce, *Chem. Soc. Rev.*, 2012, **41**, 4909.
2 Y. Rao and D. M. Antonelli, *J. Mater. Chem.*, 2009, **19**, 1937.
3 M. O. Coppens and G. F. Froment, *Fractals*, 1997, **5**, 493.
4 C. T. Kresge, M. E. Leonowicz, W. J. Roth, J. C. Vartuli and J. S. Beck, *Nature*, 1992, **359**, 710.
5 Y. Wan and D. Zhao, *Chem. Rev.*, 2007, **107**, 2821.
6 P. Feng, X. Bu, G. D. Stucky and D. J. Pine, *J. Am. Chem. Soc.*, 2000, **122**, 994.
7 J. L. Blin and M. Impéror-Clerc, *Chem. Soc. Rev.*, 2013, **42**, 4083.
8 Z. Ma, B. Zhou and Y. Ren, *Front. Environ. Sci. Eng.*, 2013, **7**, 341.
9 H. Yang and D. Zhao, *J. Mater. Chem.*, 2005, **15**, 1217.
10 Z. Wu, Q. Li, D. Feng, P. A. Webley and D. Zhao, *J. Am. Chem. Soc.*, 2010, **132**, 12042.
11 P. Wang and I. M. C. Lo, *Water Res.*, 2009, **43**, 3727.
12 M. A. Parlett, K. Wilson and A. F. Lee, *Chem. Soc. Rev.*, 2013, **42**, 3876.
13 A. Keshavaraja, V. Ramaswamy, H. S. Soni, A. V. Ramaswamy and P. Ratnasamy, *J. Catal.*, 1995, **157**, 501.
14 Y. Bai, I. Mora-Sero, F. De Angelis, J. Bisquert and P. Wang, *Chem. Rev.*, 2014, **114**, 10095.
15 Y. Ma, W. Wang, Y. Jia, X. Chen, H. Han and C. Li, *Chem. Rev.*, 2014, **114**, 9987.
16 S. Z. Islam, S. Nagpure, D. Y. Kim and S. E. Rankin, *Inorganics*, 2017, **5**, 15.
17 K. Zimny, T. Roques-Carmes, C. Carteret, M. J. Stébé and J. L. Blin, *J. Phys. Chem. C*, 2012, **116**, 6585.
18 K. Zimny, J. Ghanbaja, C. Carteret, M. J. Stébé and J. L. Blin, *New J. Chem.*, 2010, **34**, 2113.
19 M. H. Sun, S. Z. Huang, L. H. Chen, Y. Li, X. Y. Yang, Z. Y. Yuan and B. L. Su, *Chem. Soc. Rev.*, 2016, **45**, 3479.
20 Z. Y. Yuan and B. L. Su, *J. Mater. Chem.*, 2006, **16**, 663.
21 B. L. Su, C. Sanchez and X. Y. Yang, *Hierarchically Structured Porous Materials: From Nanoscience to Catalysis, Separation, Optics, Energy, and Life Science*, Wiley-VCH Verlag GmbH & Co, KGaA, Weinheim, 2011.
22 B. T. Holland, L. Abrams and A. Stein, *J. Am. Chem. Soc.*, 1999, **121**, 4308.
23 C. F. Blanford, H. Yan, R. C. Schroden, M. Al-Daous and A. Stein, *Adv. Mater.*, 2001, **13**, 401.
24 T. Sen, G. J. T. Tiddy, J. L. Casci and M. W. Anderson, *Chem. Commun.*, 2003, 2182.
25 K. Nakanishi, Y. Kobayashi, T. Amatani and K. Hirato Kodaira, *Chem. Mater.*, 2004, **16**, 3652.
26 H. Mori, M. Uota, D. Fujikawa, T. Yoshimura, T. Kuwahara, G. Sakai and T. Kijima, *Microporous Mesoporous Mater.*, 2006, **91**, 172.
27 O. Sel, D. Kuang, M. Thommes and B. Smarsly, *Langmuir*, 2006, **22**, 2311.
28 A. Imhof and D. J. Pine, *Nature*, 1997, **389**, 948.
29 J. L. Blin, R. Bleta, J. Ghanbaja and M. J. Stébé, *Microporous Mesoporous Mater.*, 2006, **94**, 74.
30 I. Naboulsi, B. Lebeau, L. Michelin, C. Carteret, L. Vidal, M. Bonne and J. L. Blin, *ACS Appl. Mater. Interfaces*, 2017, **9**, 3113.
31 R. Kimmich, *NMR: Tomography, Diffusometry, Relaxometry*, Springer, Berlin, 1997.
32 M. Thommes, K. Kaneko, A. V. Neimark, J. P. Olivier, F. Rodriguez-Reinoso, J. Rouquerol and K. S. W. Sing, *Pure Appl. Chem.*, 2015, **87**, 1051.
33 G. C. Borgia, R. J. S. Brown and P. Fantazzini, *J. Magn. Reson.*, 2000, **147**(2), 273–285.
34 M. M. Dubinin, *Progress in Surface and Membrane Science 9*, Academic Press, New York, 1975.
35 D. P. Gallegos, K. Munn, D. M. Smith and D. L. Stermer, *J. Colloid Interface Sci.*, 1986, **119**(1), 127–140.

36 F. D'Orazio, S. Bhattacharja, W. P. Halperin, K. Eguchi and T. Mizusaki, *Phys. Rev. B: Condens. Matter Mater. Phys.*, 1990, **42**(6), 9810–9818.

37 W. P. Halperin, J. Y. Hehng and Y. Q. Song, *Magn. Reson. Imaging*, 1994, **12**(2), 169–173.

38 D. Kruk and M. Florek-Wojciechowska, *Annu. Rep. NMR Spectrosc.*, 2019, **99**, chap 04.

39 E. Steiner, S. Bouguet-Bonnet, A. Robert and D. Canet, *Concepts Magn. Reson.*, 2012, **40A**(2), 80–89.

40 E. Steiner, S. Bouguet-Bonnet, J.-L. Blin and D. Canet, *J. Phys. Chem. A*, 2011, **115**, 9941–9946.

41 S. Stapf, R. Kimmich and R.-O. Seitter, *Phys. Rev. Lett.*, 1995, **75**, 2855–2858.

42 S. Stapf and R. Kimmich, *J. Chem. Phys.*, 1995, **103**, 2247–2250.

43 P. Levitz, J.-P. Korb and D. Petit, *Eur. Phys. J. E*, 2003, **12**, 29–33.

44 C. Mattea, R. Kimmich, I. Ardelean, S. Wonorahardjo and G. Farrher, *J. Chem. Phys.*, 2004, **121**, 10648–10656.

45 T. Zavada and R. Kimmich, *J. Chem. Phys.*, 1998, **109**, 6929–6939.

46 R. Kimmich, *Chem. Phys.*, 2002, **284**, 253–285.

47 P. Levitz, *J. Phys.: Condens. Matter*, 2005, **17**, S4059–S4074.

48 P. Levitz, P. A. Bonnaud, P.-A. Cazade, R. J.-M. Pellenq and B. Coasne, *Soft Matter*, 2013, **9**, 8654–8663.

49 R. Kimmich and H. Weber, *Phys. Rev. B: Condens. Matter Mater. Phys.*, 1993, **47**, 1788–11794.

50 S. Stapf, R. Kimmich and J. Niess, *J. Appl. Phys.*, 1994, **75**, 529–537.

51 T. Zavada and R. Kimmich, *Phys. Rev. E: Stat. Phys., Plasmas, Fluids, Relat. Interdiscip. Top.*, 1999, **59**, 5848–5854.

52 S. Stapf, R. Kimmich, R.-O. Seitter, A. I. Maklakov and V. D. Skirda, *Colloids Surf., A*, 1996, **115**, 107–114.

53 F. Martini, S. Borsacchi, M. Geppi, C. Forte and L. Calucci, *J. Phys. Chem. C*, 2017, **121**, 26851–26859.

54 H. Chemmi, D. Petit, J.-P. Korb, R. Denoyel and P. Levitz, *Microporous Mesoporous Mater.*, 2013, **178**, 104–107.

55 H. Chemmi, D. Petit, V. Tariel, J.-P. Korb, R. Denoyel, R. Bouchet and P. Levitz, *Eur. Phys. J.: Spec. Top.*, 2015, **224**, 1749–1768.

56 P. Sudarsanam, E. Peeters, E. V. Makshina, V. I. Parvulescu and B. F. Sels, *Chem. Soc. Rev.*, 2019, **48**, 2366–2421.

57 Y. Bai, I. Mora-Sero, F. De Angelis, J. Bisquert and P. Wang, *Chem. Rev.*, 2014, **114**, 10095–10130.

58 Y. Ma, W. Wang, Y. Jia, X. Chen, H. Han and C. Li, *Chem. Rev.*, 2014, **114**, 9987–10043.

59 K. I. Hadjiivanov and D. G. Klissurski, *Chem. Soc. Rev.*, 1996, **25**, 61–69.

60 M. Fox and M. Dulay, *Heterog. Photocatal., Chem. Rev.*, 1993, **93**, 341–357.

61 M. Hoffmann, M. S. Martin, W. Choi and D. Bahnemann, *Chem. Rev.*, 1995, **95**, 69–96.

62 Y. Zhang, Y. Zhu, A. Wang, Q. Gao, Y. Qin, Y. Chen and X. Lu, *Chin. J. Chem. Eng.*, 2019, **27**, 1403–1415.

63 C. Horch, S. Schlayer and F. Stallmach, *J. Magn. Reson.*, 2014, **240**, 24–33.

64 N. Robinson, G. Xiao, P. R. J. Connolly, N. N. A. Ling, E. O. Fridjonsson, E. F. May and M. L. Johns, *Phys. Chem. Chem. Phys.*, 2020, **22**, 13689–13697.

65 M. O. Coppens and G. F. Froment, *Fractals*, 1997, **5**, 493–505.